GEOPHYSICS, VOL. 88, NO. 6 (NOVEMBER-DECEMBER 2023); P. 1–14, 20 FIGS., 2 TABLES.
10.1190/GEO2023-0006.1

Improving vertical resolution of vintage seismic data by a weakly supervised method based on cycle generative adversarial network

Dawei Liu[1], Wenli Niu[2], Xiaokai Wang[2], Mauricio D. Sacchi[3], Wenchao Chen[2], and Cheng Wang[4]

ABSTRACT

Seismic vertical resolution is critical for accurately identifying subsurface structures and reservoir properties. Improving the vertical resolution of vintage seismic data with strongly supervised deep learning is challenging due to scarce or costly labels. To remedy the label-lacking problem, we develop a weakly supervised deep-learning method to improve vintage seismic data with poor resolution by extrapolating from nearby high-resolution seismic data. Our method uses a cycle generative adversarial network with an improved identity loss function. In addition, we contribute a pseudo-3D training data construction strategy that reduces discontinuity artifacts caused by accessing 3D field data with a 2D network. We determine the feasibility of our method on 2D synthetic data and achieve results comparable to the classic time-varying spectrum whitening method on field poststack migration data while effectively recovering more high-frequency information.

INTRODUCTION

Seismic records acquired by seismic exploration provide valuable information regarding stratigraphic structure, stratification, and fault information, particularly in the high-frequency component. However, seismic records typically need better resolution due to the decrease in frequency, primarily resulting from the following causes. On the one hand, stratum absorption leads to seismic wavelet energy attenuation, waveform broadening, and resolution reduction; on the other hand, due to the existence of multiple reflections between layers, the reflected waves of each layer will interfere with each other when they return to the surface, reducing the resolution of the collected seismic records. As high-resolution (HR) seismic data sets are essential for fine interpretations of stratigraphic structures, resolution improvement for seismic data has been extensively studied.

Traditional methods for improving seismic data resolution generally include deconvolution (Wiggins, 1978; Taylor et al., 1979; Levy and Fullagar, 1981; Sacchi, 1997; Velis, 2008; Gholami and Sacchi, 2013; Sui and Ma, 2020; Zhang et al., 2022), spectral whitening (Bian and Zhang, 1986), spectral blueing (Lancaster and Whitcombe, 2000; Kazemeini et al., 2010), and inverse Q filtering (Wang, 2006; Xue et al., 2019; Ke et al., 2023). Under certain handcrafted prior assumptions, these methods greatly increase seismic data resolution and are widely used in the industry. Despite this, their performance remains limited and cannot be substantially improved further due to the lack of prior knowledge actively derived from HR seismic data.

Recent developments in deep learning have led to a renewed interest in data-driven methods (Kaur et al., 2020; Yu and Ma, 2021; Liu et al., 2022a). The implementation of end-to-end training empowers neural networks to acquire prior knowledge directly from HR data, resulting in more effective resolution improvement than traditional methods. Especially in the image superresolution field, many classic networks (Dong et al., 2015; Kim et al., 2016a, 2016b; Mao et al., 2016a; Lai et al., 2017; Ledig et al., 2017; Tong et al., 2017; Liang et al., 2021) achieve remarkable success, contributing to the potential usefulness of deep learning to improve actual seismic data. Along with this rapid development, seismic data resolution improvement based on deep learning has received increasing attention from scholars over the past three years. Choi et al. (2019) use convolutional U-net to improve the vertical resolution of seismic data, demonstrating its benefits for thin-bed resolution. Chen et al. (2019) use an iterative deep neural network for HR seismic inversion, allowing it to estimate the wavelet and reflectivity

Manuscript received by the Editor 3 January 2023; revised manuscript received 2 July 2023; published ahead of production 12 July 2023.
[1]Xi'an Jiaotong University, School of Information and Communications Engineering, Xi'an, China and University of Alberta, Department of Physics, Edmonton, Alberta, Canada. E-mail: 409791715@qq.com.
[2]Xi'an Jiaotong University, School of Information and Communications Engineering, Xi'an, China. E-mail: 3101434366@qq.com; xkwang@xjtu.edu.cn; wencchen@xjtu.edu.cn (corresponding author).
[3]University of Alberta, Department of Physics, Edmonton, Alberta, Canada. E-mail: msacchi@ualberta.ca.
[4]Daqing Oilfield Company Ltd., the Exploration and Development Research Institute, Daqing, China. E-mail: wangcheng88@petrochina.com.cn.

simultaneously. Generative adversarial networks (GANs) are renowned for their ability to simulate data distribution autonomously. As a result, this benefit effectively addresses generative modeling problems, such as the image superresolution task. Motivated by this, Zhang et al. (2019) adopt GAN to improve seismic data resolution, which recovers more subtle and continuous reflection than traditional methods. To improve the resolution of noisy seismic data, Li et al. (2021) propose a deep network that simultaneously achieves resolution improvement and seismic denoising. To illuminate the black box and increase network interpretation, Chen et al. (2021) design an optimization-inspired deep-learning inversion solver that accelerates the solution of blind HR inverse problems. To date, studies investigating seismic resolution improvement with deep learning have primarily focused on strongly supervised deep learning, which necessitates low-resolution (LR)-HR data pairs. More concretely, achieving this requires producing HR labels that correspond precisely to LR data. However, in real-world situations, paired data are unavailable. In general, we can construct HR labels based on forward modeling or the traditional methods mentioned in the previous paragraph to mitigate this issue. The former requires accurate prior knowledge of stratigraphy, which is considerably restrictive, to produce reliable HR labels. In addition to the challenge of obtaining superior results, the latter is in a predicament because deep-learning results cannot significantly surpass the traditional methods for labeling LR data. Consequently, a contribution to research aimed at eliminating the manual construction of matching HR labels is urgently needed.

Recent research on weakly supervised learning (Jiang et al., 2021; Wei et al., 2021) provides new insights into handling signal enhancement problems with unpaired LR-HR data, thereby lessening the burden of generating hand-labeled data sets. As a famous deep network architecture, GAN is widely used to solve weakly supervised learning problems (Ignatov et al., 2018; Li et al., 2018, 2020; Wang et al., 2020a, 2020b, 2021). In addition to a forward generator and a discriminator that are implemented in the supervised GAN, weakly supervised GAN usually adopts an additional reverse generator, resulting in a cycle-in-cycle network architecture. For example, using this architecture, cycle GANs (CycleGANs) (Zhu et al., 2017), GANs that learn to discover relations between different domains (DiscoGANs) (Kim et al., 2017), and dual learning GANs (DualGANs) (Yi et al., 2017) achieve remarkable performance in image-to-image translation algorithms based on weakly supervised learning. In particular, cycle-in-cycle GAN (CinCGAN) (Yuan et al., 2018) successfully solves the single image superresolution problem with the cycle-in-cycle network architecture. As a result of significant success in the image processing field, improving image resolution without LR-HR pairs is now feasible. However, there is still uncertainty about whether weakly supervised learning can effectively recover the high-frequency component from LR seismic data.

With the development of exploration technology and HR processing technology, HR seismic data of high quality are becoming increasingly available. These HR seismic data usually involve extensive exploration costs and entail several complex processing steps, which contain rich artificial prior knowledge. It would be a significant loss if these seismic data were not properly exploited to their full potential. In contrast, vintage seismic data sets can still provide valuable underground information with better resolution. Therefore, we aim to investigate the possibility of improving LR seismic data through unpaired HR seismic data. Specifically, we propose a CycleGAN to capture the characteristics of HR seismic data and master the ability to improve the vertical resolution of LR seismic data through weakly supervised learning. For simplicity, we assume that the work area distance between the unpaired LR-HR seismic data sets is not far, so their subsurface structural features do not change significantly. Inputs to the network are LR seismic data from one work area and targets for network learning are HR seismic data from another adjacent work area. After training with the unpaired data, the network learns a distribution mapping from the LR seismic data to the HR seismic data, enabling it to extrapolate information from HR seismic data to improve the resolution of the LR vintage seismic data thereafter.

We first demonstrate the feasibility of our method on 2D synthetic data and then extend it to 3D field poststack migration data. An innovative loss function is designed by combining the latest developments in weakly supervised learning with the characteristics of 3D seismic data, which makes cross-regional training relatively stable. In addition, we introduce a pseudo-3D training data construction method by sampling randomly in the crossline and inline directions simultaneously. Compared with sampling only along a specific direction, random sampling can more effectively exploit 3D spatial features and reduce processing artifacts. The synthetic and field experiments demonstrate that the unpaired training strategy alleviates the necessity for paired label data and increases the flexibility of deep learning.

METHODS

The present research explores, for the first time, the effects of weakly supervised learning and GAN on improving the resolution of seismic data. The basic premise of our methodology is that HR improvement results for LR data should exhibit similar features and data distribution to HR data collected from a nearby survey. As a means of exploring the similarities between the LR survey and the HR survey, we adopt CycleGAN as our backbone and adapt it to our problem, as described from the three perspectives in the following. We first introduce the designed CycleGAN architecture. Then, a novel loss function tailored to the characteristics of seismic data is proposed for guiding the training process and preserving useful signal structures. Finally, we present a pseudo-3D random sampling method for building field training data. Note that the weakly supervised learning described in this paper differs from Zhou (2018), who divides weakly supervised learning into three typical types: incomplete, inexact, and inaccurate. In this paper, weak supervision is characterized as all training data with labels, but these labels are incorrect. We also refer to it as weak supervision to differentiate it from strong supervision.

Network architecture

The proposed weakly supervised learning method to improve the resolution of seismic data is accomplished with CycleGAN. As shown in Figure 1, the network framework includes a forward generator, a reverse generator, and a discriminator. The forward generator G discerns a mapping from LR data to HR data. Its input x is the LR seismic data derived from a vintage seismic data set, and its learning target y is from another HR survey. The output y' is the HR result with features similar to y. The reverse generator F simulates the reverse process of G, i.e., mapping the HR seismic data back to the original LR data to ensure the reversibility of the HR process by G. Specifically, its input is the HR output y' from G, whereas its output

x' is a degraded LR result similar to x. The discriminator D is used to evaluate and improve the generation effect of G. To distinguish the generated y' from y, D estimates a probability that y is more realistic than y'. The intention of trying to fool D directs G to synthesize HR data that are more realistic than y. By updating F, G, and D iteratively, the generator G is finally able to produce HR data y' highly similar to y. This confirms that y' achieves a reliable resolution improvement of x because the underground structure between the LR survey and its neighboring HR survey is similar.

Figure 2 shows the detailed architecture of our generator and discriminator. As shown in Figure 2a, the forward generator G and the reverse generator F use the same architecture and are trained jointly, but their parameters are updated separately. We design a 37-layer network with the following characteristics that make it more adaptable to our needs. (1) To prevent damaging useful information, there are no pooling layers included. (2) Multiresidual blocks (He et al., 2016) are used to enhance performance in deep networks. (3) The batch normalization (BN) layer is removed. The BN layer may introduce artifacts when the network becomes deeper, especially when training GAN networks, resulting in limited generalizability (Wang et al., 2018). Consequently, removing the BN layer enhances the generalization ability of the model. In addition, the removal of the BN layer helps to improve training stability and consistency. (4) The subpixel convolution layer (Shi et al., 2016) is applied to perform feature reorganization on the extracted multiple feature maps that reflect stratigraphic structure. Using the subpixel convolution layer, more contextual information can be captured through a larger receptive field, allowing for more realistic detail generation (Wang et al., 2020a, 2020b).

The discriminator architecture is shown in Figure 2b. A total of nine layers are present in the model, primarily assembled by the convolution layer, the BN layer, and the activation layer. We use leaky rectified linear unit (LeakyReLU) (Maas et al., 2013) as the activation function. In the final layer, the sigmoid activation layer is used to determine a probability between zero and one.

Loss functions

Loss functions play a crucial role in deep learning because they determine how network output is penalized during the optimization of network weights. Determining a suitable loss function that reduces prediction error and prevents overfitting is necessary. To solve the seismic resolution improvement problem, we carefully formulate the loss function in combination with the characteristics of seismic data, as described in the following two aspects: generator loss and discriminator loss.

Generator loss

The reverse and forward generators share the same network architecture, but their loss functions differ, resulting in independent parameter updates. We use an adversarial loss L_{GAN}, a cycle consistency loss L_{cyc}, an identity loss L_{idt}, and a total-variation (TV) loss L_{TV} to compose the loss function of the forward generator:

$$L_{\mathrm{Gen}} = w_1 L_{\mathrm{GAN}} + w_2 L_{\mathrm{cyc}} + w_3 L_{\mathrm{idt}} + w_4 L_{\mathrm{TV}}, \quad (1)$$

where w_1, w_2, w_3, and w_4 represent the trade-off weights assigned to each loss function. Using heuristic experiments on our testing data, we select the appropriate values for these weights, anticipating that their individual contribution to the final loss function is harmonious and collectively provides satisfactory results.

The adversarial loss is used to ensure that G provides an output that can deceive D to maximum effect; that is, y' is judged to be actual HR data by D. To stabilize the training procedure, we use the least-squares loss (Mao et al., 2016b) instead of the negative log likelihood used in Goodfellow et al. (2020). The adversarial loss is defined as

$$L_{\mathrm{GAN}} = \frac{1}{N}\sum_{i=1}^{N} \|D(G(x_i)) - 1\|_2, \quad (2)$$

where N represents the number of training samples, also called the batch size of the network training.

The cyclic consistency loss is designed to maintain consistency between x and y by ensuring the reversibility of the HR forward generator process. It is defined as

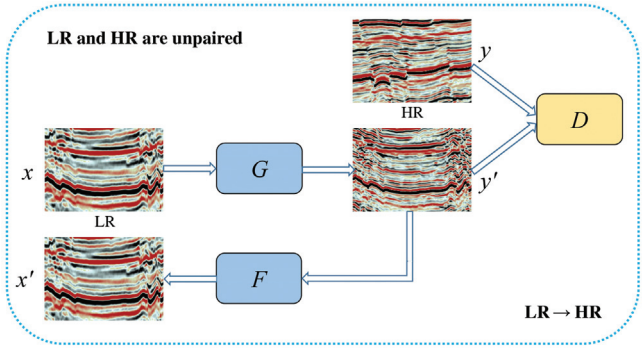

Figure 1. The proposed framework. The forward generator, the reverse generator, and the discriminator are referred to as G, F, and D, respectively. Input to G is the LR data x derived from a vintage seismic data set. Generator G attempts to produce HR data y' with features similar to the HR data y collected from another survey. Generator F maps y' to LR x' with features similar to x, ensuring that the HR process of G is reversible.

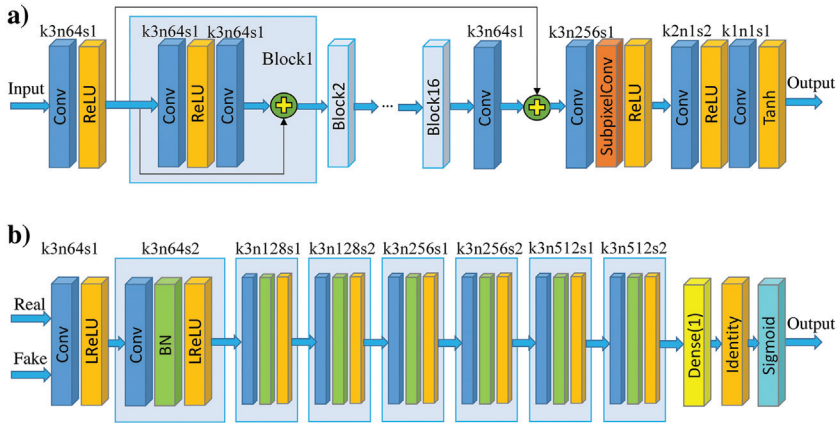

Figure 2. Network architectures. (a) This architecture applies to the forward generator G and the reverse generator F. The numbers following the terms k, n, and s denote the kernel size, the number of filters, and the stride size, respectively. (b) The architecture of the discriminator D.

$$L_{\text{cyc}} = \frac{1}{N}\sum_{i=1}^{N} \|F(G(x_i)) - x_i\|_2. \tag{3}$$

As an aside, the reverse generator F is exclusively governed by this constraint.

In the image processing field, identity loss is usually introduced to preserve color composition or maintain tint consistency between input and output images during the generation of paintings (Zhu et al., 2017). For our particular application, identity loss is used to constrain G and ensure the resolution improvement is in the correct direction. As a typical example, we can formulate it as

$$L'_{\text{idt}} = \frac{1}{N}\sum_{i=1}^{N} \|G(\bar{y}_i) - y_i\|_2, \tag{4}$$

where $\bar{y}$ denotes the LR data obtained by low-pass filtering of y. Notably, this degradation process is essential to assist G in establishing a valid mapping from LR to HR data. Not surprisingly, it is possible that this mapping deviates from the actual LR-HR mapping because the actual LR data are not low-pass filtering of existing HR data. However, it does assist G in capturing some key elements that are required to generate HR data. In addition, because other constraints exist, the final output of G is rectified by all of them simultaneously. Hence, it does not matter which degradation method is adopted to obtain $\bar{y}$, and we select low-pass filtering in this case because of its simplicity.

In addition, we incorporate the latest advances to improve identity loss further. Recent research reveals that an integrated approach with the L_1 loss and the multiscale structural similarity (MS-SSIM) loss $L_{\text{MS-SSIM}}$ leads to better image restoration results (Zhao et al., 2016). Then, we propose the following new definition of identity loss:

$$L_{\text{idt}} = \frac{1}{N}\sum_{i=1}^{N}(L_1 + L_{\text{MS-SSIM}}). \tag{5}$$

The MS-SSIM is an image quality evaluation method sensitive to local structural changes (Wang et al., 2003). The term multiscale refers to the process of downsampling an image by a factor of two after a low-pass filter is applied iteratively. Given two seismic images u and v, measurements at different scales are combined to obtain an overall MS-SSIM evaluation:

$$\begin{aligned}\text{MS}-\text{SSIM}(u,v) = {} & [l_M(u,v)]^{\alpha_M} \\ & \cdot \prod_{j=1}^{M}[c_j(u,v)]^{\beta_j}[s_j(u,v)]^{\gamma_j},\end{aligned} \tag{6}$$

where M denotes the largest scale; $l(u,v)$, $c(u,v)$, and $s(u,v)$ represent three measurements between u and v: luminance, contrast, and structure, respectively; and α, β, and γ are the corresponding weights of these three measurements and are supposed to be positive. The definitions of $l(u,v)$, $c(u,v)$, and $s(u,v)$ are, respectively,

$$\begin{aligned} l(u,v) &= \frac{2\mu_u\mu_v + c_1}{\mu_u^2 + \mu_v^2 + c_1}, \\ c(u,v) &= \frac{2\sigma_{uv} + c_2}{\sigma_u^2 + \sigma_v^2 + c_2}, \\ s(u,v) &= \frac{\sigma_{uv} + c_3}{\sigma_u\sigma_v + c_3}, \end{aligned} \tag{7}$$

where μ and σ denote the mean values and the standard deviations, respectively, and three variables c_1, c_2, and c_3 are used to stabilize the division, preventing the denominator from falling below a certain threshold. Based on MS-SSIM in equation 6, we define the MS-SSIM loss as follows:

$$L_{\text{MS-SSIM}} = \frac{1}{N}\sum_{i=1}^{N}(1\text{-MS-SSIM}(G(\bar{y}_i), y_i)). \tag{8}$$

The L_1 loss in equation 5 measures the differences between two seismic images and is calculated by

$$L_1 = \frac{1}{N}\sum_{i=1}^{N} \|G(\bar{y}_i) - y_i\|_1. \tag{9}$$

In addition, we add the TV loss to enforce spatial smoothness by avoiding extremely high gradients of the generator during the training procedure, as defined by

$$L_{\text{TV}} = \frac{1}{N}\sum_{i=1}^{N}(\|\nabla_h G(x_i)\|_2 + \|\nabla_w G(x_i)\|_2), \tag{10}$$

where ∇_h and ∇_w are the functions used to determine the horizontal and vertical gradient of $G(x)$, respectively.

Discriminator loss

Following the core idea of GAN, we rely on the discriminator D for adversarial training G. More concretely, the loss function of D is used to ensure that D can correctly determine the difference between real and fake HR data. It judges the actual HR data y to be authentic and outputs one, whereas the generator's output y' is deemed fake and outputs zero. For this purpose, we define it as follows (Mao et al., 2016b):

$$L_{\text{Dis}} = \frac{1}{N}\sum_{i=1}^{N}(\|D(G(x_i)) - 0\|_2 + \|D(y_i) - 1\|_2). \tag{11}$$

To summarize, the optimization of G follows the minimization of equation 1, the optimization of F relies on equation 3, and the optimization of D is conducted by minimizing equation 11. Using these equations, G, F, and D are optimized alternately during the training process.

Joint random sampling for training data set construction

In most cases, poststack seismic data requiring resolution improvement are a 3D data set. Intuitively, 3D networks (Wu et al., 2019; Liu et al., 2022b; Saad et al., 2022) would be superior to 2D networks in capturing 3D seismic features and delivering better results. However,

two apparent difficulties arise when applying 3D networks to weakly supervised resolution improvement. On the one hand, 3D networks involve a greater number of network parameters, thus requiring substantial training data; otherwise, overfitting is likely to occur due to insufficient training data. Unfortunately, vintage LR data typically have small data volumes because of old-fashioned exploration technology, further aggravating this problem. On the other hand, 3D networks are computationally expensive and often involve days of training, making hyperparameter tuning very challenging. Therefore, we use the alternative approach, 2D networks, to operate on 3D data and perform resolution enhancement.

Processing 3D data with 2D profile-by-profile methods often results in discontinuities along the profile's normal direction, which also occurs with 2D networks. Taking 3D poststack denoising as an example, if the 2D network is trained on inline profiles, it performs well on inline profiles but introduces discontinuity artifacts on crossline profiles, and vice versa (Liu et al., 2020). This indicates that a standard 2D training method is insufficient to provide the desired adaptivity on a global scale. Similarly, we encounter this problem when improving the resolution of 3D field data with the proposed 2D network. Figure 3a shows the LR seismic profile of a field 3D data set that requires resolution improvement using the proposed weakly supervised method. First, we train our network with profiles only along inline directions, which is consistent with the original profile shown in Figure 3a. The testing results are shown in Figure 3b, which evidently yields a higher resolution with continuous and coherent events. Unfortunately, when we examine the testing results from the other direction, e.g., concerning the crossline profile shown in Figure 4a, evident discontinuities in events can be observed, as indicated by the yellow boxes in Figure 4b. These discontinuities, also characterized by oscillation smearing, deblur the events, making it more difficult to track horizons and identify faults. It is evident that this problem is caused by dimension reduction during 2D training, in which coherency among inline sections is ignored. To leverage this previously ignored information, we propose a straightforward but effective training data sampling method, i.e., randomly sampling along inline and crossline axes. In contrast to the previous single-direction view of the data set, our method can be regarded as a valuable data augment, gaining access to the entire data set from multiple perspectives. This data augmentation does not require the same cropping positions for input and target sections, offering more flexibility than previous sampling strategies for paired training data (Alaudah et al., 2019; Hamida et al., 2022). Figures 3c and 4c verify the success of the proposed method in the resolution improvement. More importantly, we avoid the previous discontinuities in either crossline or inline profiles. Note that all parameters, including the sample number N, remained the same in the preceding comparison, except for the sampling method used for generating training data. Please refer to the "Real data experiment" section for more details regarding data set information and experimental parameter settings.

EXPERIMENTS AND RESULTS

In this section, we first demonstrate the feasibility of our model based on unpaired data training using a 2D synthetic data example. Then, we evaluate the performance of the proposed network on field data sets to improve the resolution of an LR vintage data set by a local HR data set. In addition, the validity of our method is

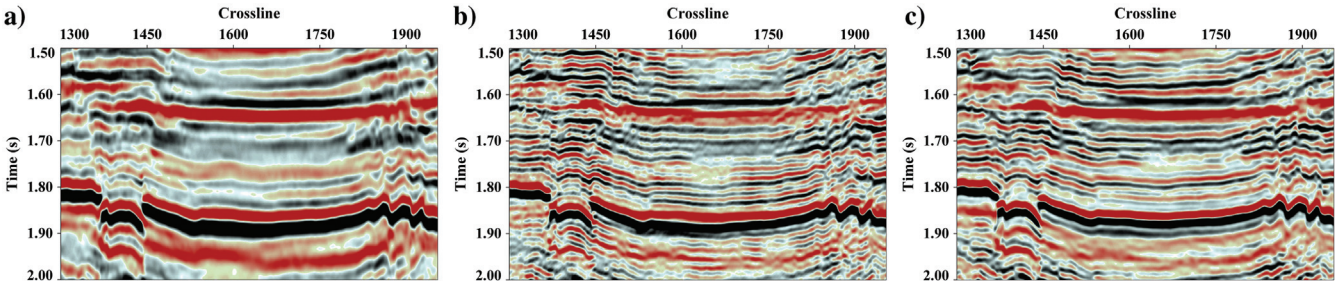

Figure 3. Inline profile comparison of 2D network testing results for different sampling methods. (a) Original LR seismic data. (b) Testing results when training samples are randomly cropped solely from profiles along the inline axis. (c) Testing results when training samples are randomly cropped from profiles along inline and crossline axes.

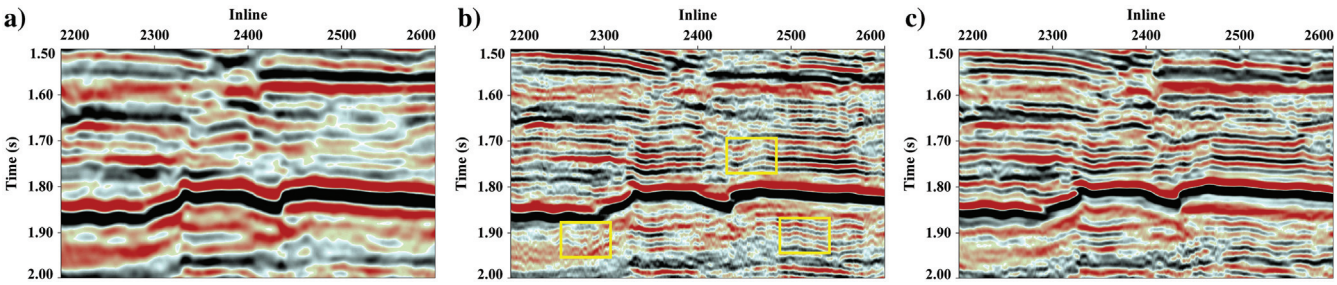

Figure 4. Crossline profile comparison of 2D network testing results for different sampling methods. (a) Original LR seismic data. (b) Testing results when training samples are randomly cropped solely from profiles along the inline axis. As indicated by the yellow boxes, there is a disruption in the continuity of events. (c) Testing results when training samples are randomly cropped from profiles along inline and crossline axes.

confirmed by comparison with the traditional time-varying spectrum whitening method.

Synthetic data experiment

Synthetic data generation

We use the Marmousi2 model (Martin et al., 2006) to conduct synthetic experiments. The 2D synthetic seismic data are generated by the convolution of wavelets and reflection coefficients derived from P-wave velocity and density. Here, we adopt the Ormsby wavelet (Ormsby, 1961), a band-pass wavelet, to generate seismic data with different resolutions. The parameters f_{L1}, f_{L2}, f_{H1}, and f_{H2} represent the low-cut, low-pass, high-pass, and high-cut frequencies of the Ormsby wavelet, respectively. They are in increasing order and given here in Hertz.

Training data construction

The purpose of this experiment is to simulate the situation for a weakly supervised learning approach under the premise of unpaired LR-HR data. Accordingly, following these procedures, we synthesize two types of synthetic data: vintage data from an LR seismic field and training targets from an HR seismic field. The parameters of the band-pass wavelet for generating LR data are (f_{L1}, f_{L2}, f_{H1}, f_{H2}) = (1, 4, 15, 18). For generating HR data, we set the parameters of the band-pass wavelet to (f_{L1}, f_{L2}, f_{H1}, f_{H2}) = (1, 4, 24, 27). The resulting data profiles have a size of 3311 × 13601 (depth × distance). We select the left half of the synthetic LR seismic data as the input data, as shown in the yellow rectangular box in Figure 5a, and the right half of the synthetic HR seismic data as the training targets, as shown in the yellow rectangular box in Figure 5b.

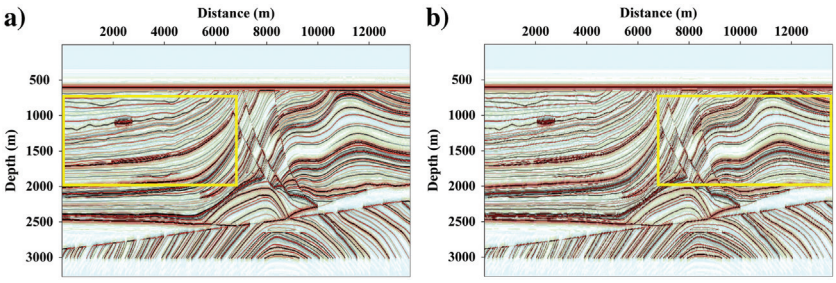

Figure 5. Data segments for two training areas: (a) the LR data obtained by the band-pass wavelet of (1, 4, 15, 18) and (b) the HR data obtained by the band-pass wavelet of (1, 4, 24, 27). As indicated by the yellow boxes, we regard the left half of the LR data as source data and the right half of the HR data as target data.

Training details

We train our model with the Adam optimizer (Kingma and Ba, 2014) by setting $\beta_1 = 0.5$, $\beta_2 = 0.999$, and $\varepsilon = 10^{-8}$, without weight decay. Training samples are randomly cropped from the rectangular regions in the synthetic seismic profiles using uniformly distributed sampling for simplicity. The four parameters in equation 1 are defined as $w_1 = 1$, $w_2 = 10$, $w_3 = 5$, and $w_4 = 0.5$, respectively. The network training parameters are set as follows. The patch size is 96×96, the initial learning rate is 0.0002 with an exponential decay rate of 0.5, the decay period is 100 epochs, the batch size is 16, and the total number of training epochs is 600. During the training, we randomly select a portion of the training sample pairs (1600 pairs) from the specified areas instead of using all of them. As the training data and the label are unpaired, we regenerate new training sample pairs every 200 epochs, based on our empirical testing, to ensure training stability and feature diversity. Finally, we feed them to the network for training in batches.

Evaluation of results

Enhancing high-frequency features while preserving low-frequency information is essential for effectively improving resolution. To measure the effectiveness of our proposed method on synthetic data, we assess the results from two perspectives: the profile results and the multitrace average amplitude spectrum.

We first examine the results in the left half of the synthetic seismic data, as shown in Figure 6. Our method effectively improves the resolution of the synthetic LR data and restores valuable detailed information. Overall, the results are as accurate as the HR convolution model generated by HR wavelets, particularly at strong-energy events. A detailed comparison of the results outside the training areas is shown in Figure 7. The areas indicated by the yellow arrows demonstrate that our method provides more precise structural information, and the events are smoother than simulated HR data, illustrating better lateral continuity. The stratigraphic sequence structure has not changed, indicating the reliability of this technique. The red arrow areas show that our method also effectively improves the resolution of weak events in synthetic LR data. These results provide convincing evidence of the benefits offered by the complex mapping ability of the network.

Then, we observe the results in the right half area in Figure 8. Our approach significantly improves seismic resolution even for complex structures and weak-energy events, exhibiting

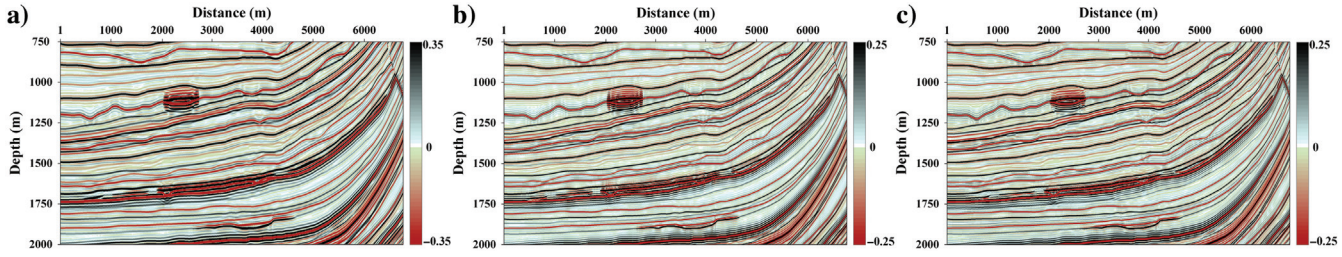

Figure 6. Result comparison for the left half area of the LR synthetic data: (a) original LR data, (b) the HR data obtained by the convolution model, and (c) the HR data obtained by our method.

impressive generalization ability. Furthermore, the enlarged results in Figure 9 show that our method obtains clearer and more continuous events than the synthetic HR data in the yellow arrow areas. Similarly, in the red arrow areas, our method achieves results close to the simulated HR data, especially in areas where the event is difficult to separate. To quantitatively assess the similarity of our method to the HR convolution model, we use two standard metrics: the Pearson correlation coefficient (PCC) and the signal-to-noise ratio (S/N). The obtained PCC is 0.9749 and the output S/N of our method is 12.24 dB, indicating that our approach yields accurate HR results.

Furthermore, we investigate the LR outputs of the reverse generator F to demonstrate that our network architecture is reasonable and the cycle structure is conducive to our network. Comparing Figure 10a and 10b, we observe relatively similar structures, indicating that the HR results generated by our method can be reverted to the original LR space. Figure 10c also demonstrates a minor difference between them. In addition, by examining Figure 11, we can verify that the reverse generator of our network can effectively accomplish the opposite function of the forward generator. Our LR output achieves a PCC of 0.9823 and an S/N of 13.92 dB compared with the original LR convolution model, demonstrating the successful mastery of the mutual distribution transition between the LR and HR data by our network.

Finally, we analyze the multitrace average amplitude spectrums, as shown in Figure 12. Our method obtains spectrums close to the synthetic HR data, regardless of whether the spectrums are derived from the left, right, or entire areas. The proposed technique effectively expands the bandwidth of the synthetic LR data and recovers the high-frequency information without damaging the low-frequency useful information. In addition, the reversal outputs of the HR results obtained by our method are reasonably close to the amplitude spectrum of the synthetic LR data, which further verifies the reversibility of our method.

Real data experiment

Data set description

The LR and HR data used in this study are two 3D poststack migration records acquired by dynamite from different work areas

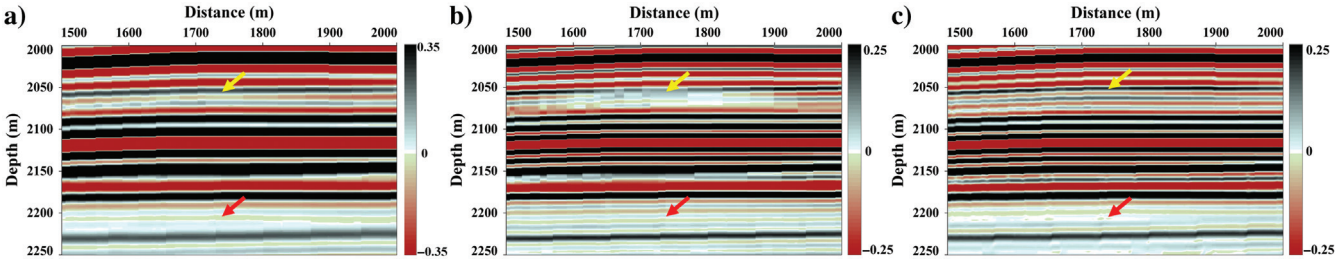

Figure 7. Enlarged result comparison for the left half area of the LR synthetic data: (a) original LR data, (b) the HR data obtained by the convolution model, and (c) the HR data obtained by our method. As indicated by the yellow arrows, our method can obtain more continuous events than synthetic HR data. Weak-energy events are also improved, according to the red arrows.

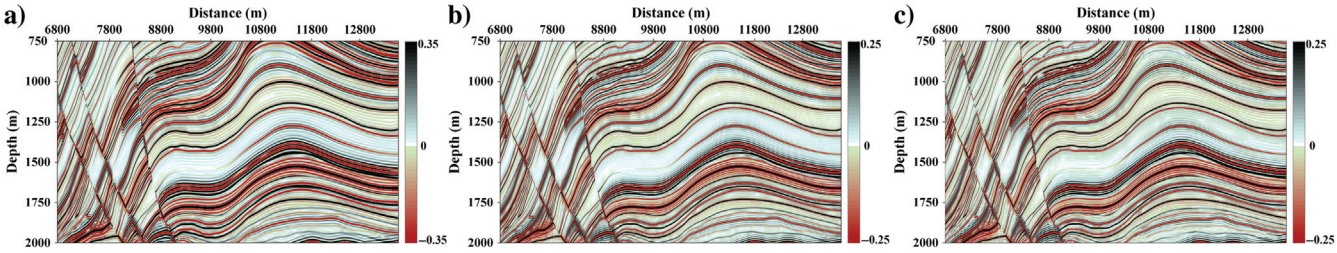

Figure 8. Result comparison for the right half area of the LR synthetic data: (a) original LR data, (b) the HR data obtained by the convolution model, and (c) the HR data obtained by our method.

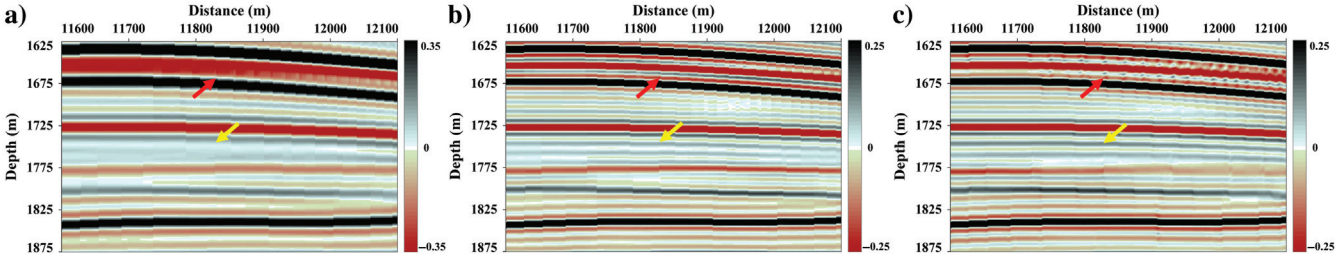

Figure 9. Enlarged result comparison for the right half area of the LR synthetic data: (a) original LR data, (b) the HR data obtained by the convolution model, and (c) the HR data obtained by our method. As indicated by the yellow arrows, our method can obtain clearer structural information than synthetic HR data. Weak-energy events are improved significantly, according to the red arrows.

of the Daqing Oilfield, which are approximately 30 km apart. The LR data have been collected in 1995 with equipment and acquisition parameters typical of that time. There are 401 survey lines in the work area, and each survey line has 661 receivers. The detailed parameters are as follows. The total time length is 4 s, the sampling frequency is 250 Hz, the bin size is 25 m × 50 m, the fold number is 20, and the aspect ratio is 0.32. Even after advanced merging processing, the resolution remains unsatisfactory due to the limitations of acquisition technology during that period. The HR data have been collected in 2016 with an HR processing procedure. There are 401 survey lines in the work area, and each line has 371 sampling points. The time window length is also 4 s with a sampling frequency of 250 Hz, the same as the LR data. Notably, the fold number is 240 and the aspect ratio is 0.79, indicating a wide-azimuth and high-density 3D seismic survey. Accordingly, the bin size is 10 m × 20 m, smaller than the LR data. In addition to data acquisition technology, HR processing technology has made significant progress since 1995, facilitating the availability of HR seismic data. The data sets are normalized before training to ensure that the relative reflected energy at different positions remains unchanged, but their training sizes and areas may be different because the input data and training targets are not paired.

Training data

The yellow boxes shown in Figure 13 indicate the selected training area, which covers approximately 64% of the total data set. The window length is from 800 to 2200 ms in the time direction. The

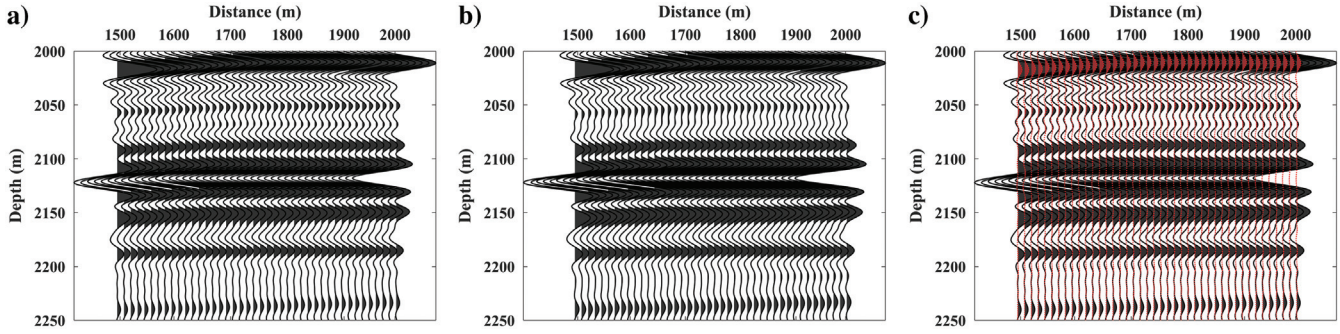

Figure 10. Reversibility assessment for the left half area of the LR synthetic data: (a) original LR data, (b) LR outcomes obtained by the reverse generator *F*, and (c) differences (the red wiggles adhered to the original LR wiggles) between (a) and (b).

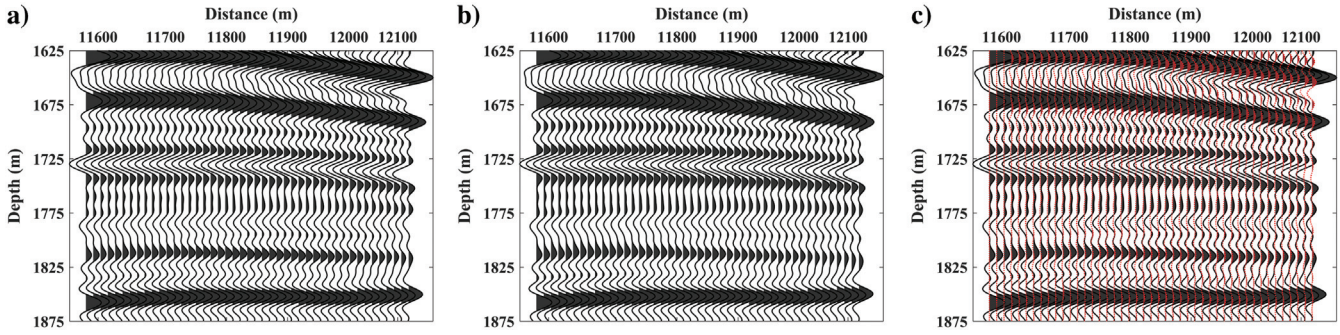

Figure 11. Reversibility assessment for the right half area of the LR synthetic data: (a) original LR data, (b) LR outcomes obtained by the reverse generator *F*, and (c) differences (the red wiggles adhered to the original LR wiggles) between (a) and (b).

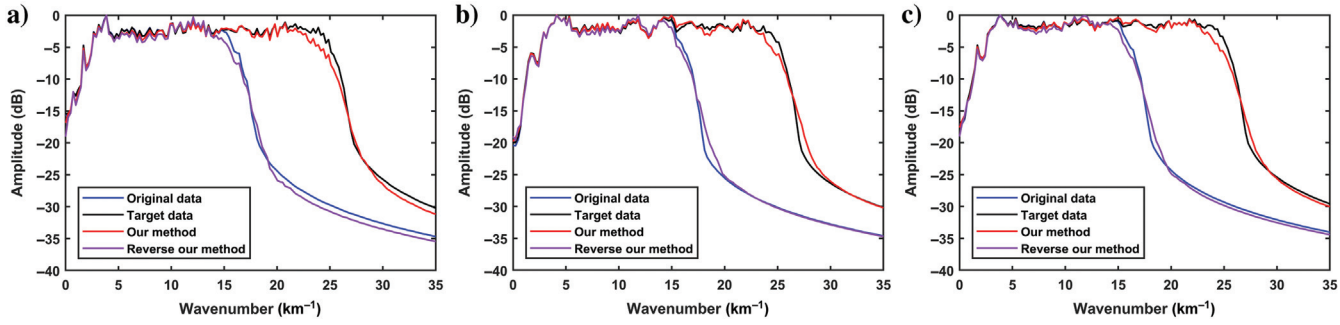

Figure 12. Multitrace average amplitude spectrum analysis for (a) the left half area, (b) the right half area, and (c) the whole area of the synthetic data.

input data differ significantly from the learning targets in size and structure, highlighting the mismatched training samples for weakly supervised learning. Even though it is highly challenging for conventional methods, the proposed network improves the resolution of the entire LR data set when trained with these unpaired data.

Figure 14 shows the contrast between the LR input data and the HR learning targets in profiles, whose positions are indicated by the blue lines in Figure 13, as well as the corresponding multitrace average amplitude spectrums. The profiles reveal significant resolution differences between the LR input data and the HR learning targets, with the input data having severely limited resolution compared with the HR learning targets. The multitrace average amplitude spectrums also demonstrate a substantial mismatch in frequency distribution between the input data and the learning targets. The input data have narrow frequency bands and lack high-frequency energy, whereas the learning targets have relatively wide frequency bands with prevalent high-frequency energy. The apparent distribution mismatch between the unpaired training data highlights the strong transition capability in weakly supervised learning.

Training details

As described in the previous section, we use the joint random sampling method to reduce the discontinuities that naturally arise when using a 2D network to process 3D data. Training sample pairs are randomly sampled along the inline and crossline directions with a size of 96×96. The four parameters in equation 1 are set to be $w_1 = 1$, $w_2 = 10$, $w_3 = 5$, and $w_4 = 2$, respectively. The following are the remaining parameters. The initial learning rate is 0.0002, which then exponentially decays every 100 epochs with a decay rate of 0.5; the batch size is 16; the number of training epochs is 800 and each epoch includes 1600 sample pairs; and new training samples are selected from the training area every 200 epochs.

Results analysis

We evaluate the performance of the proposed method from four aspects: a crossline profile, an inline profile, time slices, and multitrace average amplitude spectrums. To further verify the accuracy and effectiveness in improving resolution, the proposed method is compared with the traditional time-varying spectrum whitening technique that is widely implemented in the industry.

We first examine the inline profile results, as shown in Figure 15. Compared with the original profile shown in Figure 14a, both methods significantly improve seismic data resolution and recover useful information. In general, our results have a consistent event structure compared with the traditional method, verifying the rationality of our results. Moreover, our method provides higher accuracy in determining stratigraphic structure relationships due to higher spatial consistency. Specifically, the yellow arrows in Figure 15 indicate that the proposed method provides better lateral continuity. A closer examination of the crossline results in Figure 16 supports these findings. It is challenging for the traditional time-varying spectrum whitening method to maintain the spatial continuity and energy consistency of the prominent reflection event, as indicated by the yellow arrows. In contrast, our method produces higher-resolution results with better lateral continuity. In addition, both methods effectively preserve the low-frequency useful information of the original seismic data, as demonstrated by the multitrace average amplitude spectrum in the bottom right corner, where the blue, black, and red lines represent the original LR seismic data, the HR results obtained by the traditional time-varying spectrum whitening method, and the HR results obtained by our method, respectively.

Then, we analyze the multitrace average amplitude spectrums of each profile by gathering them into Figure 17. The traditional and our methods significantly increase the effective bandwidth and enhance the high-frequency information with similar improvement levels. In addition, our method better fits the trend pattern of the

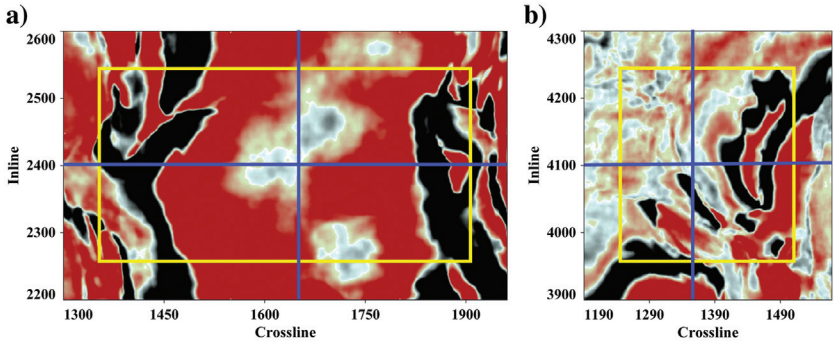

Figure 13. Training areas: (a) the LR input data and (b) the HR learning targets. The yellow boxes indicate the selected training area, whereas the blue lines delineate the areas for visualizing the profile results subsequently.

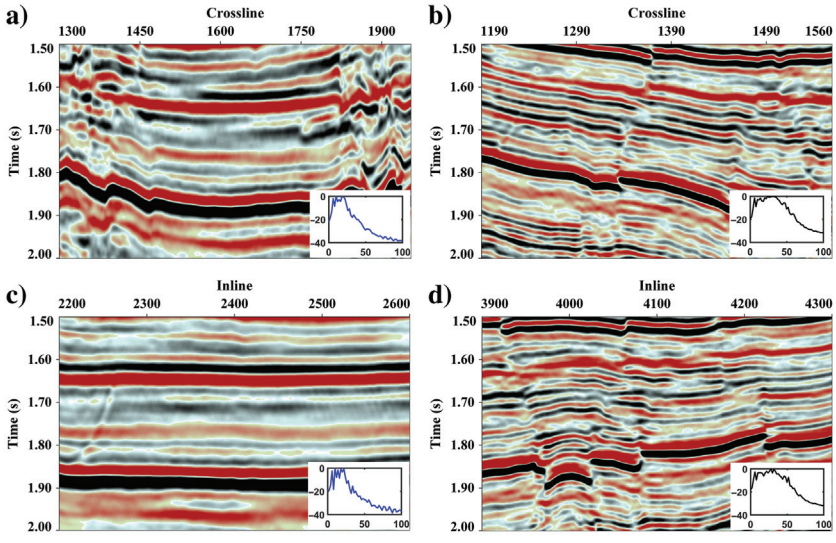

Figure 14. Example comparison of the inline and crossline profiles between the input data and the training targets. The multitrace average amplitude spectrum of each profile is displayed in the bottom right corner. (a) The LR input data at inline 2400, (b) the HR targets at inline 4100, (c) the LR input data at crossline 1650, and (d) the HR targets at crossline 1350.

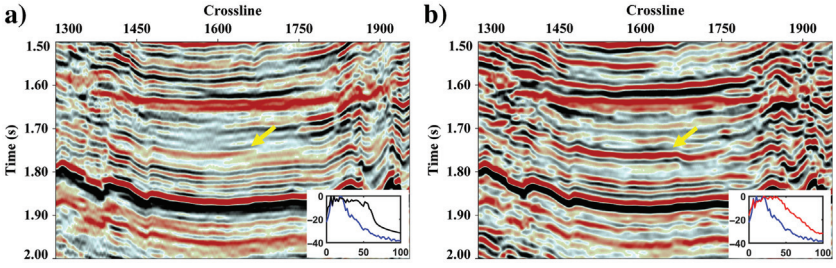

Figure 15. Inline profile results obtained by (a) the traditional time-varying spectrum whitening method and (b) the proposed method (for the raw LR data, see Figure 14a). The multitrace average amplitude spectrum of each profile is displayed in the bottom right corner. The yellow arrows indicate that our method offers better spatial consistency for events.

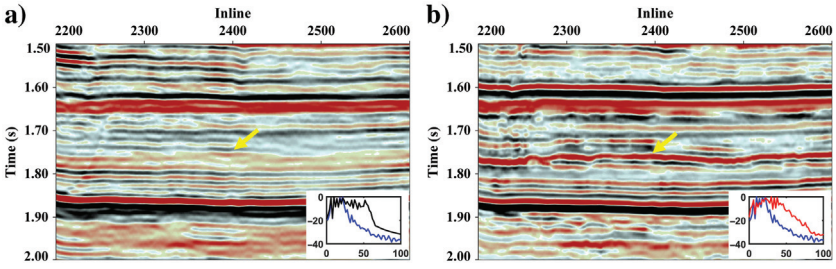

Figure 16. Crossline profile results obtained by (a) the traditional time-varying spectrum whitening method and (b) the proposed method (for the raw LR data, see Figure 14c). The multitrace average amplitude spectrum of each profile is displayed in the bottom right corner. Our method produces higher resolution results, as indicated by the yellow arrows.

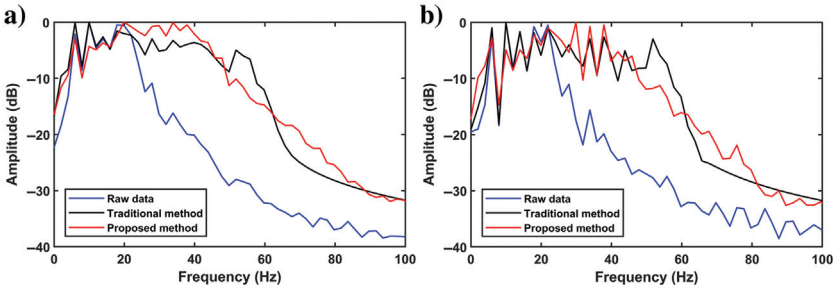

Figure 17. Multitrace average amplitude spectrum analysis for (a) the profile of inline 2400 and (b) the profile of crossline 1350.

original data in the low-frequency range, indicating a higher preservation of useful information.

To further examine the effectiveness of our method, we display the results on two time slices. In the time slice at 1750 ms (Figure 18), our method shows higher resolution and better recovery of events with stronger energy and more detailed structural information. Particularly in the yellow boxes, the stratigraphic structure is more accurately depicted with our method, and the spatial relationship between the strata is more clearly described by revealing richer details. Figure 19 shows a comparison of the time slice at 1850 ms. On further analysis of the areas indicated by the yellow and white ellipses, we can draw a similar conclusion to Figure 18 that our method recovers credible HR data.

To verify the reliability and fidelity of our proposed method, we generate synthetic seismic data using acoustic and density logging data from a well at crossline 1492. Figure 20 shows that the traditional time-varying spectrum whitening method and our proposed method produce HR results that match well with the synthetic data at peaks and troughs with strong amplitude. However, our method not only captures waveform trends and characteristics similar to the synthetic data but also reveals more details and clearly illustrates fractures that are critical for accurate geologic interpretation. Quantitatively, our method achieves a high level of accuracy with a correlation coefficient of 0.66, outperforming the original LR data (0.61) and the baseline method (0.58). This high reliability facilitates the accurate recovery of thin layers and weak reflection amplitudes.

DISCUSSION

Ablation study

To illustrate the advantages of the proposed loss function for the semisupervised resolution improvement, we conduct an ablation study on 2D synthetic data. The impact of different loss functions is evaluated with PCC and output S/N

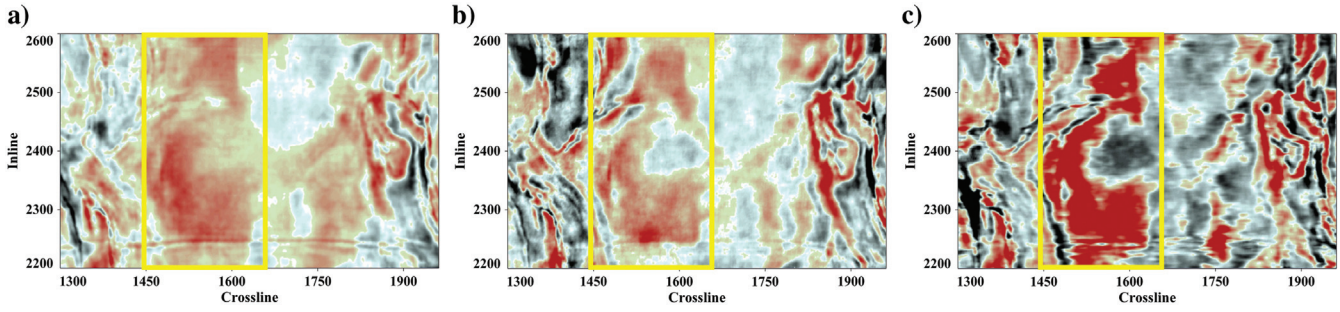

Figure 18. Comparison of time-slice results at 1750 ms: (a) the LR seismic data, (b) the HR result obtained by the traditional time-varying spectrum whitening method, and (c) the HR result obtained by our method. The comparison of the yellow boxes indicates that the stratigraphic structure is more accurately depicted with our method.

metrics, as shown in Table 1. The results indicate that our proposed approach, which uses a combination of L_{GAN}, L_{cyc}, L_{idt}, and L_{TV}, outperforms the networks trained without these loss functions. Specifically, removing L_{GAN}, L_{cyc}, and L_{TV} leads to a slight decrease in performance, whereas the omission of L_{idt} causes a substantial decrease in PCC and output S/N. Consequently, the identity loss function is the most critical component, as it determines the training direction, whereas the other loss functions further enhance its performance in a subsidiary manner. These findings highlight the importance of using a combination of loss functions to improve the model's performance for resolution enhancement tasks. In addition, the last line of Table 1 indicates that replacing the original L'_{idt} with our proposed L_{idt} is justifiable, as it leads to improved PCC and S/N scores.

Remaining challenge and future work

The proposed network is trained on a novel strategy that uses an unpaired training data set and presents excellent high-frequency reconstruction capabilities, even for complex structures and weak-energy events. This approach assumes that the two data sets have similar underground structural features and provides a flexible way to leverage this prior knowledge for resolution improvement. We also contribute an improved loss function and sample selection method to make it applicable to field data. However, obtaining representative training data remains a challenge. In our field example, we successfully use two data sets that were 30 km apart but determining the maximum distance for applying this method still requires more

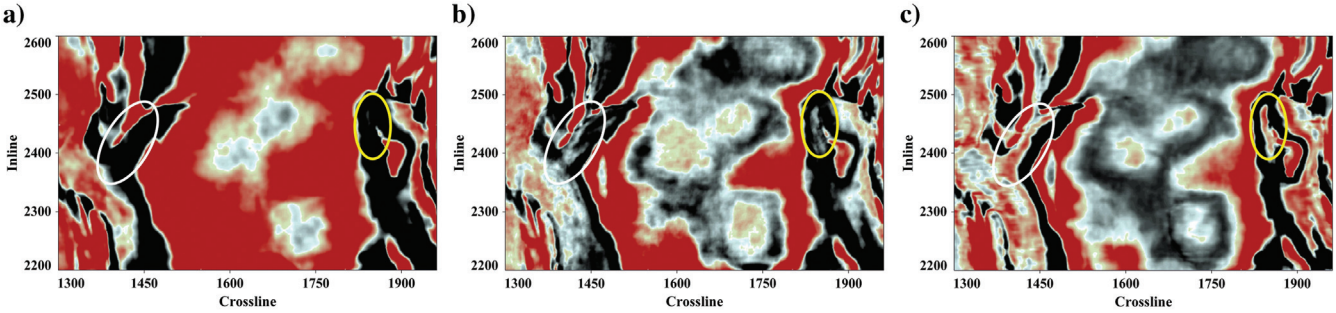

Figure 19. Comparison of time-slice results at 1850 ms: (a) the LR seismic data, (b) the HR result obtained by the traditional time-varying spectrum whitening method, and (c) the HR result obtained by our method. By comparing the yellow and white ellipses, it can be observed that our method recovers credible HR data.

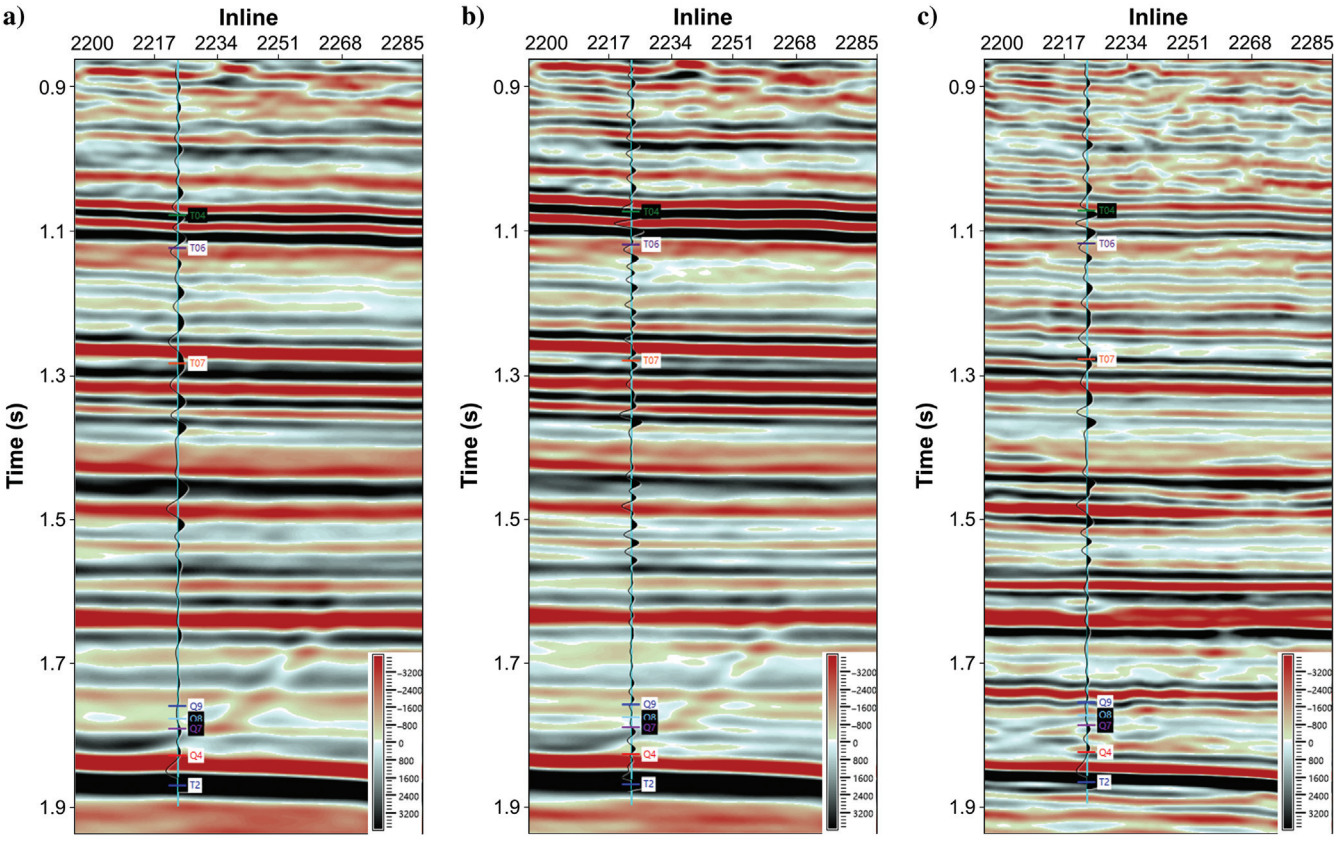

Figure 20. Comparison of well-to-seismic tie results in crossline 1492: (a) the LR seismic data, (b) the HR result obtained by the traditional time-varying spectrum whitening method, and (c) the HR result obtained by our method.

practical experience. For other practical applications, factors such as the survey type used to acquire the data, subsurface geologic conditions, and seismic source wavelets should be considered when selecting appropriate training data. In addition, one limiting factor is that the proposed method is only applicable when the LR and HR data sets have similar geologic features and cannot be applied in situations with entirely different patterns. For instance, if the LR data set contains prevalent strike-slip faults, whereas the HR data set does not, the output HR results will eliminate these faults as noise, producing unrealistic results. In addition, because our method draws inspiration from image superresolution and focuses mainly on improving high-frequency components, it still has limitations on low-frequency components. Accordingly, another critical factor for data selection is that the LR-HR data set pairs should have similar low cutoff frequencies, which are crucial pattern features. If the low-cutoff frequency components are not matched, the output HR results will shrink or extend the low-frequency accordingly, potentially resulting in inaccurate lineups.

Noise analysis is essential for seismic data resolution improvement. We conduct additional experiments on synthetic data with varying noise levels and include the results in Table 2. The findings suggest that our method performs well with moderate levels of noise. However, as is widely recognized, deep learning is vulnerable and has inherent limitations in its robustness ability, and strong noise can still have a notable impact, especially for accurately reconstructing thin-layer structures. Our proposed training strategy presents a novel but more challenging scenario, further exacerbating this issue. The strong amplitude and wide-bandwidth noise may distract our network and cause it to pay more attention to high-frequency noise components, thereby deviating from the useful information representing the strata. As a result, applying our method to prestack data remains challenging.

Nevertheless, our method's performance on noisy data is acceptable, given our goal of improving the resolution of poststack migration data, which typically contains less noise. To address the resolution improvement under severe noise conditions, one intuitive approach is to include an extra denoising module that maps the noisy LR data to a noise-free LR space (Yuan et al., 2018). In addition, using a pretrained model on a denoising data set or adding noise to the current training data also helps the model learn to be more robust to noise.

These challenges require further investigation to refine the proposed approach and expand its applicability. Nevertheless, we believe our approach has significant potential for broad applications. Another promising application involves improving the resolution of deep-layer data by learning from the shallow-layer data of the same data set. Their same acquisition method, similar low-frequency range, and similar noise level make them well suited for our proposed approach.

Table 1. Comparison of different ablation settings.

Loss function	PCC	Output S/N (dB)
Our	0.9749	12.24
Without L_{GAN}	0.9573	9.79
Without L_{cyc}	0.9483	9.58
Without L_{idt}	0.8284	4.83
Without L_{TV}	0.9624	10.99
With L'_{idt}	0.9663	11.63

The PCC and output S/N are calculated to measure the similarity between y' produced by G and the HR learning target y.

Table 2. Comparison of the proposed method regarding different input noise levels.

Input S/N (dB)	PCC	Output S/N (dB)
∞ (clean)	0.9749	12.24
30	0.9742	12.16
25	0.9721	11.93
20	0.9588	10.69
15	0.8992	6.92

The input S/N is calculated against the LR synthetic data x to evaluate the input noise levels, whereas the PCC and output S/N are calculated to measure the distance between y' and y.

CONCLUSION

This study offers a fresh perspective on seismic resolution improvement via CycleGAN in a weakly supervised manner. Because seismic data from neighboring surveys have highly similar features, the proposed method uses unpaired local data for training, thus eliminating the necessity to obtain paired labels. Specifically, the proposed method learns cycle mappings between two unpaired LR and HR data sets, which then can be applied to enhance the resolution of LR seismic data. To achieve this, we carefully design the loss function in conjunction with the characteristics of seismic data. Moreover, a joint random sampling approach is introduced to reduce artifacts when implementing the 2D network to process 3D data. Experiments on synthetic and real seismic data are carried out to test the feasibility and effectiveness of the developed method. Compared with the traditional time-varying spectrum whitening method, our method recovers more high-frequency information and has better spatial continuity and consistency. Due to the high flexibility of weakly supervised learning, our results can be further boosted by providing more sophisticated HR data.

ACKNOWLEDGMENTS

This research is sponsored by the National Natural Science Foundation of China (41974131). The work of D. Liu was supported by the China Scholarship Council. We thank the assistant editor Y. Liu, the anonymous associate editor, and the reviewers for their insightful suggestions. We also thank K. Guo and H. Chen for their helpful discussion on field data.

DATA AND MATERIALS AVAILABILITY

Data associated with this research are available and can be obtained by contacting the corresponding author.

REFERENCES

Alaudah, Y., P. Michałowicz, M. Alfarraj, and G. AlRegib, 2019, A machine-learning benchmark for facies classification: Interpretation, **7**, no. 3, SE175–SE187, doi: 10.1190/INT-2018-0249.1.

Bian, G., and L. Zhang, 1986, Spectral whitening of seismic data: Geophysical Prospecting for Petroleum, **2**, 26–33.
Chen, D., J. Gao, Y. Hou, and Z. Gao, 2019, High resolution inversion of seismic wavelet and reflectivity using iterative deep neural networks: 89th Annual International Meeting, SEG, Expanded Abstracts, 2538–2542, doi:10.1190/segam2019-3216178.1.
Chen, H., J. Gao, X. Jiang, Z. Gao, and W. Zhang, 2021, Optimization-inspired deep learning high-resolution inversion for seismic data: Geophysics, **86**, no. 3, R265–R276, doi: 10.1190/geo2020-0034.1.
Choi, Y., S. J. Seol, J. Byun, and Y. Kim, 2019, Vertical resolution enhancement of seismic data with convolutional U-net: 89th Annual International Meeting, SEG, Expanded Abstracts, 2388–2392, doi:10.1190/segam2019-3216042.1.
Dong, C., C. C. Loy, K. He, and X. Tang, 2015, Image super-resolution using deep convolutional networks: IEEE Transactions on Pattern Analysis and Machine Intelligence, **38**, 295–307, doi: 10.1109/TPAMI.2015.2439281.
Gholami, A., and M. D. Sacchi, 2013, Fast 3D blind seismic deconvolution via constrained total variation and GCV: SIAM Journal on Imaging Sciences, **6**, 2350–2369, doi: 10.1137/130905009.
Goodfellow, I., J. Pouget-Abadie, M. Mirza, B. Xu, D. Warde-Farley, S. Ozair, A. Courville, and Y. Bengio, 2020, Generative adversarial networks: Communications of the ACM, **63**, 139–144, doi: 10.1145/3422622.
Hamida, A., M. Alfarraj, A. A. Al-Shuhail, and S. A. Zummo, 2022, Efficient seismic image super-resolution: Second International Meeting for Applied Geoscience & Energy, SEG, Expanded Abstracts, 1659–1663, doi: 10.1190/image2022-3746892.1.
He, K., X. Zhang, S. Ren, and J. Sun, 2016, Deep residual learning for image recognition: Proceedings of the IEEE Conference on Computer Vision and Pattern Recognition, 770–778.
Ignatov, A., N. Kobyshev, R. Timofte, K. Vanhoey, and L. Van Gool, 2018, WESPE: Weakly supervised photo enhancer for digital cameras: Proceedings of the IEEE Conference on Computer Vision and Pattern Recognition Workshops, 691–700.
Jiang, Y., X. Gong, D. Liu, Y. Cheng, C. Fang, X. Shen, J. Yang, P. Zhou, and Z. Wang, 2021, EnlightenGAN: Deep light enhancement without paired supervision: IEEE Transactions on Image Processing, **30**, 2340–2349, doi: 10.1109/TIP.2021.3051462.
Kaur, H., N. Pham, and S. Fomel, 2020, Improving the resolution of migrated images by approximating the inverse Hessian using deep learning: Geophysics, **85**, no. 4, WA173–WA183, doi: 10.1190/geo2019-0315.1.
Kazemeini, S. H., C. Yang, C. Juhlin, S. Fomel, and C. Cosma, 2010, Enhancing seismic data resolution using the prestack blueing technique: An example from the Ketzin CO_2 injection site, Germany: Geophysics, **75**, no. 6, V101–V110, doi: 10.1190/1.3483900.
Ke, X., Y. Shi, X. Fu, L. Song, H. Jing, J. Yang, and Z. Zhang, 2023, The nth power Fourier spectrum analysis for the generalized seismic wavelets: IEEE Transactions on Geoscience and Remote Sensing, **61**, 1–10, doi: 10.1109/TGRS.2023.3243184.
Kim, J., J. K. Lee, and K. M. Lee, 2016a, Deeply recursive convolutional network for image super-resolution: Proceedings of the IEEE Conference on Computer Vision and Pattern Recognition, 1637–1645.
Kim, J., J. K. Lee, and K. M. Lee, 2016b, Accurate image super-resolution using very deep convolutional networks: Proceedings of the IEEE Conference on Computer Vision and Pattern Recognition, 1646–1654.
Kim, T., M. Cha, H. Kim, J. K. Lee, and J. Kim, 2017, Learning to discover cross-domain relations with generative adversarial networks: International Conference on Machine Learning, 1857–1865.
Kingma, D. P., and J. Ba, 2014, Adam: A method for stochastic optimization: arXiv Preprint, doi: 10.48550/arXiv.1412.6980.
Lai, W.-S., J.-B. Huang, N. Ahuja, and M.-H. Yang, 2017, Deep Laplacian pyramid networks for fast and accurate super-resolution: Proceedings of the IEEE Conference on Computer Vision and Pattern Recognition, 624–632.
Lancaster, S., and D. Whitcombe, 2000, Fast-track 'coloured' inversion: 80th Annual International Meeting, SEG, Expanded Abstracts, 1572–1575, doi: 10.1190/1.1815711.
Ledig, C., L. Theis, F. Huszár, J. Caballero, A. Cunningham, A. Acosta, A. Aitken, A. Tejani, J. Totz, Z. Wang, and W. Shi, 2017, Photo-realistic single image super-resolution using a generative adversarial network: Proceedings of the IEEE Conference on Computer Vision and Pattern Recognition, 4681–4690.
Levy, S., and P. K. Fullagar, 1981, Reconstruction of a sparse spike train from a portion of its spectrum and application to high-resolution deconvolution: Geophysics, **46**, 1235–1243, doi: 10.1190/1.1441261.
Li, C., J. Guo, and C. Guo, 2018, Emerging from water: Underwater image color correction based on weakly supervised color transfer: IEEE Signal Processing Letters, **25**, 323–327, doi: 10.1109/LSP.2018.2792050.
Li, J., X. Wu, and Z. Hu, 2021, Deep learning for simultaneous seismic image super-resolution and denoising: IEEE Transactions on Geoscience and Remote Sensing, **60**, 1–11, doi: 10.1109/TGRS.2021.3057857.
Li, Y., H. Wang, and X. Dong, 2020, The denoising of desert seismic data based on cycle-GAN with unpaired data training: IEEE Geoscience and Remote Sensing Letters, **18**, 2016–2020, doi: 10.1109/LGRS.2020.3011130.
Liang, J., J. Cao, G. Sun, K. Zhang, L. Van Gool, and R. Timofte, 2021, SwinIR: Image restoration using swin transformer: Proceedings of the IEEE/CVF International Conference on Computer Vision, 1833–1844.
Liu, D., W. Wang, X. Wang, Z. Shi, M. D. Sacchi, and W. Chen, 2022b, Improving sparse representation with deep learning: A workflow for separating strong background interference: Geophysics, **88**, no. 1, WA253–WA266, doi: 10.1190/geo2022-0179.1.
Liu, D., W. Wang, X. Wang, C. Wang, J. Pei, and W. Chen, 2020, Poststack seismic data denoising based on 3-D convolutional neural network: IEEE Transactions on Geoscience and Remote Sensing, **58**, 1598–1629, doi: 10.1109/TGRS.2019.2947149.
Liu, D., X. Wang, X. Yang, H. Mao, M. D. Sacchi, and W. Chen, 2022a, Accelerating seismic scattered noise attenuation in offset-vector tile domain: Application of deep learning: Geophysics, **87**, no. 5, V505–V519, doi: 10.1190/geo2021-0654.1.
Maas, A. L., A. Y. Hannun, and A. Y. Ng, 2013, Rectifier nonlinearities improve neural network acoustic model: ICMLWorkshop on Deep Learning for Audio, Speech and Language Processing.
Mao, X., Q. Li, H. Xie, R. Y. Lau, and Z. Wang, 2016b, Multi-class generative adversarial networks with the L2 loss function: arXiv Preprint, doi: 10.48550/arXiv.1611.04076.
Mao, X., C. Shen, and Y.-B. Yang, 2016a, Image restoration using very deep convolutional encoder-decoder networks with symmetric skip connections: Advances in Neural Information Processing Systems, 29.
Martin, G. S., R. Wiley, and K. J. Marfurt, 2006, Marmousi2: An elastic upgrade for Marmousi: The Leading Edge, **25**, 156–166, doi: 10.1190/1.2172306.
Ormsby, J. F., 1961, Design of numerical filters with applications to missile data processing: Journal of the ACM, **8**, 440–466, doi: 10.1145/321075.321087.
Saad, O. M., Y. A. S. I. Oboué, M. Bai, L. Samy, L. Yang, and Y. Chen, 2022, Self-attention deep image prior network for unsupervised 3-D seismic data enhancement: IEEE Transactions on Geoscience and Remote Sensing, **60**, 1–14, doi: 10.1109/TGRS.2021.3108515.
Sacchi, M. D., 1997, Reweighting strategies in seismic deconvolution: Geophysical Journal International, **129**, 651–656, doi: 10.1111/j.1365-246X.1997.tb04500.x.
Shi, W., J. Caballero, F. Huszár, J. Totz, A. P. Aitken, R. Bishop, D. Rueckert, and Z. Wang, 2016, Real-time single image and video super-resolution using an efficient sub-pixel convolutional neural network: Proceedings of the IEEE Conference on Computer Vision and Pattern Recognition, 1874–1883.
Sui, Y., and J. Ma, 2020, Blind sparse-spike deconvolution with thin layers and structure: Geophysics, **85**, no. 6, V481–V496, doi: 10.1190/geo2019-0423.1.
Taylor, H. L., S. C. Banks, and J. F. McCoy, 1979, Deconvolution with the $\ell 1$ norm: Geophysics, **44**, 39–52, doi: 10.1190/1.1440921.
Tong, T., G. Li, X. Liu, and Q. Gao, 2017, Image super-resolution using dense skip connections: Proceedings of the IEEE International Conference on Computer Vision, 4799–4807.
Velis, D. R., 2008, Stochastic sparse-spike deconvolution: Geophysics, **73**, no. 1, R1–R9, doi: 10.1190/1.2790584.
Wang, H., Y. Li, and X. Dong, 2020a, Generative adversarial network for desert seismic data denoising: IEEE Transactions on Geoscience and Remote Sensing, **59**, 7062–7075, doi: 10.1109/TGRS.2020.3030692.
Wang, X., L. Xie, C. Dong, and Y. Shan, 2021, Real-ESRGAN: Training real-world blind super-resolution with pure synthetic data: IEEE/CVF International Conference on Computer Vision Workshops, 1905–1914.
Wang, X., K. Yu, S. Wu, J. Gu, Y. Liu, C. Dong, Y. Qiao, and C. C. Loy, 2018, ESRGAN: Enhanced super-resolution generative adversarial networks: European Conference on Computer Vision, 63–79.
Wang, Y., 2006, Inverse Q-filter for seismic resolution enhancement: Geophysics, **71**, no. 3, V51–V60, doi: 10.1190/1.2192912.
Wang, Z., J. Chen, and S. C. Hoi, 2020b, Deep learning for image super-resolution: A survey: IEEE Transactions on Pattern Analysis and Machine Intelligence, **43**, 3365–3387, doi: 10.1109/TPAMI.2020.2982166.
Wang, Z., E. P. Simoncelli, and A. C. Bovik, 2003, Multiscale structural similarity for image quality assessment: 37th Asilomar Conference on Signals, Systems & Computers, 1398–1402.
Wei, Y., Z. Zhang, Y. Wang, M. Xu, Y. Yang, S. Yan, and M. Wang, 2021, DerainCycleGAN: Rain attentive CycleGAN for single image deraining and rainmaking: IEEE Transactions on Image Processing, **30**, 4788–4801, doi: 10.1109/TIP.2021.3074804.
Wiggins, R. A., 1978, Minimum entropy deconvolution: Geoexploration, **16**, 21–35, doi: 10.1016/0016-7142(78)90005-4.
Wu, X., L. Liang, Y. Shi, and S. Fomel, 2019, FaultSeg3D: Using synthetic data sets to train an end-to-end convolutional neural network for 3D seismic fault segmentation: Geophysics, **84**, no. 3, IM35–IM45, doi: 10.1190/geo2018-0646.1.

Xue, Y.-J., J.-X. Cao, and X.-J. Wang, 2019, Inverse Q filtering via synchrosqueezed wavelet transform: Geophysics, **84**, no. 2, V121–V132, doi: 10.1190/geo2018-0177.1.
Yi, Z., H. Zhang, P. Tan, and M. Gong, 2017, DualGAN: Unsupervised dual learning for image-to-image translation: Proceedings of the IEEE International Conference on Computer Vision, 2849–2857.
Yu, S., and J. Ma, 2021, Deep learning for geophysics: Current and future trends: Reviews of Geophysics, **59**, e2021RG000742, doi: 10.1029/2021RG000742.
Yuan, Y., S. Liu, J. Zhang, Y. Zhang, C. Dong, and L. Lin, 2018, Unsupervised image super-resolution using cycle-in-cycle generative adversarial networks: IEEE/CVF Conference on Computer Vision and Pattern Recognition Workshops, 701–710.
Zhang, H., W. Wang, X. Wang, W. Chen, Y. Zhou, C. Wang, and Z. Zhao, 2019, An implementation of the seismic resolution enhancing network based on GAN: 89th Annual International Meeting, SEG, Expanded Abstracts, 2478–2482, doi: 10.1190/segam2019-3216229.1.
Zhang, Y., H. Zhou, Y. Wang, M. Zhang, B. Feng, and W. Wu, 2022, A novel multichannel seismic deconvolution method via structure-oriented regularization: IEEE Transactions on Geoscience and Remote Sensing, **60**, 1–10, doi: 10.1109/TGRS.2022.3141113.
Zhao, H., O. Gallo, I. Frosio, and J. Kautz, 2016, Loss functions for image restoration with neural networks: IEEE Transactions on Computational Imaging, **3**, 47–57, doi: 10.1109/TCI.2016.2644865.
Zhou, Z.-H., 2018, A brief introduction to weakly supervised learning: National Science Review, **5**, 44–53, doi: 10.1093/nsr/nwx106.
Zhu, J.-Y., T. Park, P. Isola, and A. A. Efros, 2017, Unpaired image-to-image translation using cycle-consistent adversarial networks: Proceedings of the IEEE International Conference on Computer Vision, 2223–2232.

Biographies and photographs of the authors are not available.